ADVANCED FUNCTIONAL MATERIALS
www.afm-journal.de



# Long-Range Domain Structure and Symmetry Engineering by Interfacial Oxygen Octahedral Coupling at Heterostructure Interface

*Zhaoliang Liao, Robert J. Green, Nicolas Gauquelin, Sebastian Macke, Lin Li, Julie Gonnissen, Ronny Sutarto, Evert P. Houwman, Zhicheng Zhong, Sandra Van Aert, Johan Verbeeck, George A. Sawatzky, Mark Huijben, Gertjan Koster,* and Guus Rijnders*

**In epitaxial thin film systems, the crystal structure and its symmetry deviate from the bulk counterpart due to various mechanisms such as epitaxial strain and interfacial structural coupling, which is accompanyed by a change in their properties. In perovskite materials, the crystal symmetry can be described by rotations of sixfold coordinated transition metal oxygen octahedra, which are found to be altered at interfaces. Here, it is unraveled how the local oxygen octahedral coupling at perovskite heterostructural interfaces strongly influences the domain structure and symmetry of the epitaxial films resulting in design rules to induce various structures in thin films using carefully selected combinations of substrate/buffer/film. Very interestingly it is discovered that these combinations lead to structure changes throughout the full thickness of the film. The results provide a deep insight into understanding the origin of induced structures in a perovskite heterostructure and an intelligent route to achieve unique functional properties.**

## 1. Introduction

Diverse electronic phases in solid state materials such as superconductivity, topological insulating phases, and ferroelectricity are intimately coupled to crystal symmetry.[1–5] Controlled symmetries have been extensively employed in oxide heterostructures for generating novel properties and functionalities.[6–11] In $ABO_3$ perovskites, the crystal symmetry resides in the corner sharing oxygen octahedral ($BO_6$) network.[2,12–14] These symmetries, or oxygen octahedral rotation (OOR) patterns in perovskite heterostructures, are often engineered by epitaxial strain.[15] Furthermore, the required connectivity of the octahedra across the heterostructure interface enforces a geometric constraint to the 3D octahedral network in epitaxial films.[16–21] The control of this oxygen octahedral coupling (OOC) at interfaces has been shown to result in interesting phenomena in ultrathin oxide films.[17–21] However, the effect of the OOC on octahedral tilt angles decays away from the interface and is found to be confined to layer thicknesses of only 4–8 unit cells (uc).[17–21] The short range impact of the OOC on the tilt angle was recently further demonstrated for $La_{2/3}Sr_{1/3}MnO_3$ (LSMO)/$NdGaO_3$ (NGO) heterostructure, in which the OOC driven novel anisotropic properties only emerge in LSMO thinner than 8 uc.[17] The limited propagation of the interface-induced octahedral tilt into the film currently restricts the engineering of perovskite heterostructures with unique functional properties.

Changing the strain or substrate symmetry are two well-known strategies to long range engineer the lattice structures and in most situations they cooperatively affect the film structures.[22–27] However, how exactly the substrate symmetry plays a role distinguished from strain is still an open question. A very typical question is why an orthorhombic (110) substrate such

Dr. Z. L. Liao, Dr. L. Li, Dr. E. P. Houwman, Dr. M. Huijben, Prof. G. Koster, Prof. G. Rijnders
MESA+ Institute for Nanotechnology
University of Twente
P. O. BOX 217, 7500 AE, Enschede, The Netherlands
E-mail: g.koster@utwente.nl
Dr. R. J. Green, Dr. S. Macke, Prof. G. A. Sawatzky
Quantum Matter Institute and Department of Physics and Astronomy
University of British Columbia
2355 East Mall, Vancouver V6T 1Z4, Canada
Dr. R. J. Green
Max Planck Institute for Chemical Physics of Solids
Nöthnitzerstraße 40, 01187 Dresden, Germany
Dr. N. Gauquelin, Dr. J. Gonnissen, Prof. S. Van Aert, Prof. J. Verbeeck
Electron Microscopy for Materials Science (EMAT)
University of Antwerp
2020 Antwerp, Belgium
Dr. S. Macke, Dr. Z. Zhong
Max Planck Institute for Solid State Research
Heisenbergstraße 1, 70569 Stuttgart, Germany
Dr. R. Sutarto
Canadian Light Source
Saskatoon, Saskatchewan S7N 2V3, Canada

**DOI: 10.1002/adfm.201602155**

as $NdGaO_3$ (110) can give rise to single domain structure of an orthorhombic film.[23,24] Even in the case that the films such as $BiFeO_3$ have rhombohedral symmetry, the orthorhombic substrates still favor formation of only two specific domains among the four possible rhombohedral structure domains. Since the strain between substrate and different domains is identical, the interfacial symmetry mismatch rather than lattice mismatch is proposed to play a central role.[23,27] However, the microscopic mechanism of symmetry mismatch effect is still not clear. By systematically investigating the effect of substrate symmetry on film structures while maintaining the same lattice stain, we unravel the important role of interfacial OOC in determining the film domain structure. We further show that the OOC can even induce a new symmetry in the film and this new symmetry can propagate away from the interface deeply into the full thickness of the films. Our results indicate that the OOC induced rotational behavior in-phase or out-of-phase can survive over a much longer range compated to the OOC induced octahedral tilt angle.

## 2. Results and Discussion

The symmetry of a perovskite is reflected by the characteristic OOR throughout the crystal, which is usually described using the Glazer notation.[12] For example, a Glazer notation $c^+a^-a^-$ corresponds to the orthorhombic Pbnm structure. The Glazer letters hereafter are sequentially corresponding to the rotation about the pseudocubic *a*, *b*, and *c*-axes, respectively. For a detailed study of specific OOC effects at interfaces a more precise description of the rotations of each octahedron is required. Therefore, the interfacial OOR in a perovskite is redefined by a network of rotation signs of the individual octahedra by using the clockwise and counterclockwise rotation along specific crystal axes as negative (–) and positive (+), respectively, and no rotation as zero (0), as shown in **Figure 1**a which shows the 3D oxygen octahedral connections. The required connectivity of octahedra strictly restricts the adjacent rotation signs, as illustrated by an example of a single tilt system in Figure 1b, where adjacent octahedra residing in a plane normal to the tilt axis require opposite rotation signs about that axis. Further, the in-phase or out-of-phase rotation designations restrict the rotation signs of adjacent octahedra along the tilt axis, taking Figure 1c as an example for out-of-phase rotation. Therefore, the rotation behavior of each individual octahedron is fully correlated to that of its neighbor by these two octahedral connectivity rules. For a triple octahedral tilt system, the rotation of each individual octahedron has three components of rotation about three pseudocubic axes and the rotation of an octahedron is characterized by three rotation signs, i.e., (± ± ±), about *a*, *b*, and *c*-axis, respectively (see Figure 1d). The characteristic Glazer tilt system can be visualized by drawing a rotation signs network of eight octahedra from a unit cell, in which for example a front-bottom-left octahedron with a specific rotation sign fully determines the

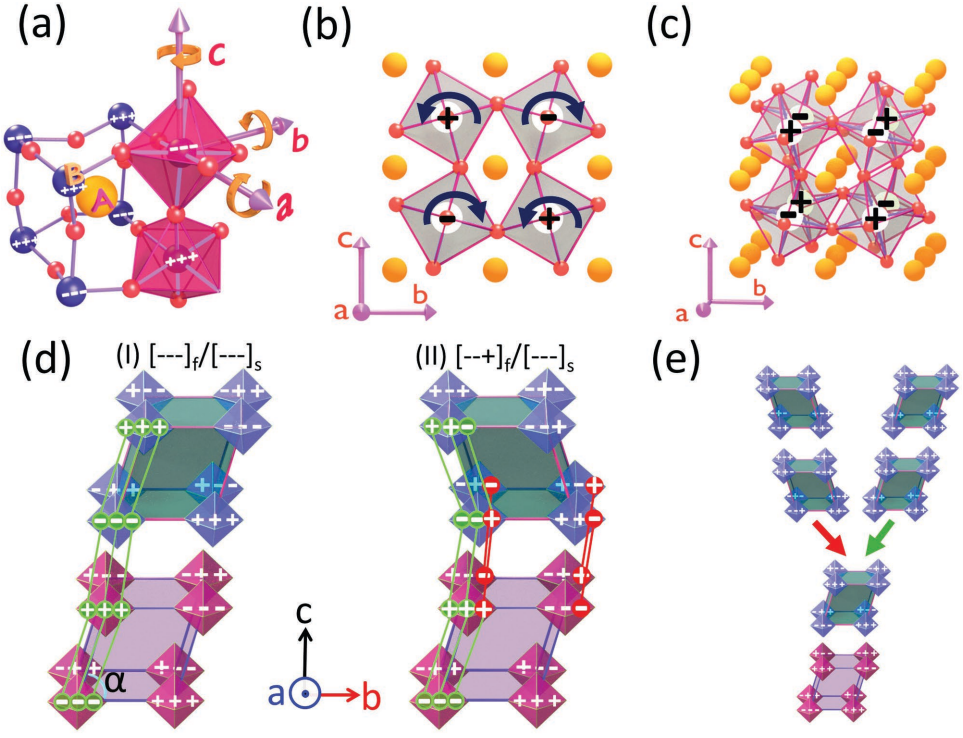


**Figure 1.** OOC initiated structure at interface. a) The definition of the rotation sign of an individual octahedron in an $ABO_3$ perovskite unit cell with clockwise (+) and anticlockwise (–). The letters A and B indicate the A-site and B-site atoms, respectively. b) Rotation sign patterns of octahedra in a shared rotation axis normal plane. c) Requirement of the adjacent rotation signs along a tilt axis in order to comply with the out-of-phase rotation designations. d) Rotation signs network across CTO/NGO interface. (I) and (II) show the $[---]_f/[---]_s$ and $[--+]_f/[---]_s$ configurations, respectively. The green "⊷" highlight some of the matched tilt signs while all the unmatched tilt signs are highlighted by red "⊷". e) The symmetry constraint shown in panel (d) is enforced to every subsequent layer. Green and red arrows indicate the preferred and unpreferred growth, respectively.



*Adv. Funct. Mater.* **2016**,
DOI: 10.1002/adfm.201602155

whole network. For simplicity, the rotation sign of the front-bottom-left octahedron is used to represent the whole rotation network, e.g., [−−−] for the bottom rotation signs network in Figure 1dI. Disregarding the relative difference in the magnitude of the tilts, the $c^+a^-a^-$ and $a^+a^-a^-$ actually have the same rotation pattern and we will focus on the rotation signs network by simplifying the Glazer notation to $a^+a^-a^-$. There are only two possible rotation networks for $a^+a^-a^-$: the [−−−] and the [−−+] networks, which corresponds to two orthorhombic structure domains with lattice angles $\alpha$ and 180–$\alpha$, respectively (see Section I, Supporting Information). Taking $CaTiO_3$ (CTO) as an example, the [−−−] and [−−+] networks produce $\alpha < 90°$ and $\alpha > 90°$, respectively (see Figure 1dI,II).[28]

There are two possible resultant structures when coherently growing an orthorhombic perovskite film (f) on an orthorhombic perovskite $(110)_{orth}$ substrate (s): either $[---]_f/[---]_s$, or $[--+]_f/[---]_s$ (see Figure 1d). Since the $[--+]_f$ is the mirror of $[---]_f$ with respect to the *ac* plane, the $[--+]_f$ and $[---]_f$ share exactly the same lattice mismatch with substrate along both the *a* and *b*-axis, the strain effect cannot distinguish the two growth configurations. However, the octahedral connectivity across interface is different. The interface of $[---]_f/[---]_s$ naturally maintains an $a^+a^-a^-$ symmetry across the interface, while $[--+]_f/[---]_s$ interface violates the two octahedral connectivity rules mentioned above (for more detail, see Figure S1, Supporting Information). To maintain the connectivity of the octahedra, the former is expected to be energetically more favorable, because less octahedral distortion is required to connect the octahedra. Since the symmetry constraints are enforced to every subsequent layer, the structure initiated at the interface propagates deeper into the film (see Figure 1e). This analysis is confirmed experimentally in the study of CTO/NGO heterostructures, in which CTO[28] and NGO[29] share the same $c^+a^-a^-$ structure with [−−−] for $\alpha < 90°$ and [−−+] for $\alpha > 90°$. The unit cell structure of a 30 uc thick CTO film on NGO $(110)_{orth}$ was determined by X-ray reciprocal space mapping (RSM) of the (0-24), (024), (204), (–204) reflections as shown in **Figure 2**a. Details of the growth of the films can be found in Figure S2 and Table S1, Supporting Information. The characteristic symmetric peaks between (204) and (–204) and nonsymmetric peaks between (0–24) and (024) indicate an orthorhombic structure in CTO with in-phase rotation along *a*-axis.[15] The lattice angles $\beta$ and $\gamma$ both are 90° and $\alpha$ is determined as $\frac{\pi}{2} - \tan^{-1}\left(\frac{(0\bar{2}4)_z - (024)_z}{2*(024)_x}\right)$ (see Figure S3, Supporting Information), yielding for our film $\alpha_{CTO} = 89.38°$. The determined $\alpha_{CTO} < 90°$ on $\alpha_{NGO} < 90°$ structure configuration by RSM suggests that the $[---]_f/[---]_s$ interface is energetically more favorable than $[--+]_f/[---]_s$

Further strong evidence for OOC mediated epitaxial growth is found in the resultant structure of a $SrRuO_3$ (SRO) film on a $DyScO_3$ (DSO) $(110)_{orth}$ substrate. Similar to NGO, the [−−−] network of DSO corresponds to $\alpha < 90°$,[30] whereas one has $\alpha > 90°$ for the [−−−] network of SRO.[31] The difference in unit cell tilt directions is caused by the different orthorhombic distortions (see Figure S4, Supporting Information). Therefore, we still expect a $[---]_f/[---]_s$ growth but with an $\alpha_{SRO} > 90°$ on $\alpha_{DSO} < 90°$ structural configuration for SRO/DSO, which is consistent with experimental observation (see Figure 2b). The RSM of a 30 uc SRO film on DSO shows that $\alpha$ of the SRO film is 90.57°.

In an interface between two perovskites with the same symmetry (homosymmetric) such as CTO/NGO and SRO/DSO, the OORs can be perfectly matched, hence the resulting OOC effect breaks the mirror symmetry and induces a single domain structure with a single monoclinic tilt direction. In contrast, OORs cannot be matched across an interface between materials with different symmetries (heterosymmetric), e.g., the interface between rhombohedral ($a^-a^-a^-$) $BiFeO_3$ (BFO) and an orthorhombic ($a^+a^-a^-$) substrate. The BFO has four possible rotation networks: $r_4$ $[---]_{rhom}$, $r_1$ $[+--]_{rhom}$, $r_2$ $[--+]_{rhom}$ and $r_3$ $[+-+]_{rhom}$[25,32] all of which have mismatched rotation signs at an interface with a $[---]_{orth}$ substrate (see **Figure 3**a). However, different networks have different degrees of mismatch with $[---]_{orth}$. The $[---]_{rhom}$ and $[+--]_{rhom}$ networks have the same degree of mismatch with the $[---]_{orth}$ network in that they both have 2 tilt signs violating the first rule at the interface about the *a*-axis, hence the $[---]_{rhom}$ and $[+--]_{rhom}$ are equally favored for epitaxial growth. The $[--+]_{rhom}$ and $[+-+]_{rhom}$ on $[---]_{orth}$ also have an equal degree of mismatch and thus are equally favored for epitaxial growth, but they have an additional 4 tilt signs violating the second rule about the *c*-axis besides 2 tilt signs violating the first rule about the *a*-axis. Therefore, the $[---]_{rhom}/[---]_{orth}$ and $[+--]_{rhom}/[---]_{orth}$ interfaces with less octahedral mismatch are expected to be energetically more favorable than the $[--+]_{rhom}/[---]_{orth}$ and $[+-+]_{rhom}/[---]_{orth}$ interfaces during growth. Experimentally, it has been widely reported before by several groups that the $r_4$ ($[---]_{rhom}$) and $r_1$ ($[+--]_{rhom}$) domains are energetically more favorable when BFO films are grown on orthorhombic $REScO_3$ (RSO) (RE = Dy, Gd, Tb) and SRO $(110)_{orth}$ substrates (see Figure 3b).[25–27] The different structure configurations of $\alpha_{BFO} < 90°$ on $\alpha_{RSO} < 90°$ versus $\alpha_{BFO} < 90°$ on $\alpha_{SRO} > 90°$ are due to the fact that the RSO and SRO possess $\alpha < 90°$ and $\alpha > 90°$ respectively for the same $[---]_{orth}$ network. In conclusion, the domain structures of BFO on different orthorhombic substrates are uniformly explained by the interfacial OOC effect.

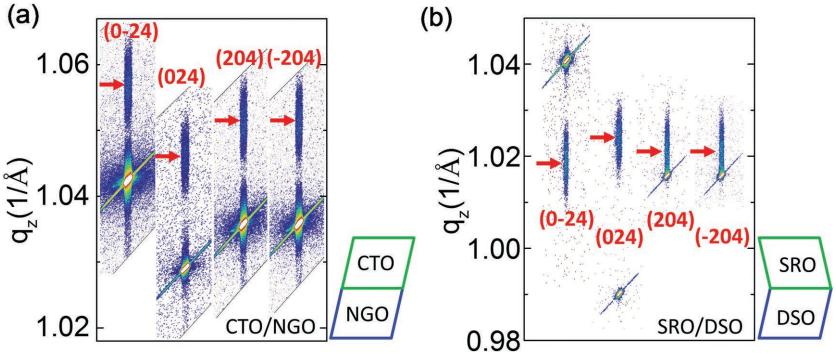


**Figure 2.** Interface-OOC-driven single domain structure in orthorhombic films. RSM of (0-24), (024), (204) and (–204) reflections for a) 30 uc CTO/NGO and b) 30 uc SRO/DSO. The film peaks are indicated by arrows and the brightest peaks come from substrate.

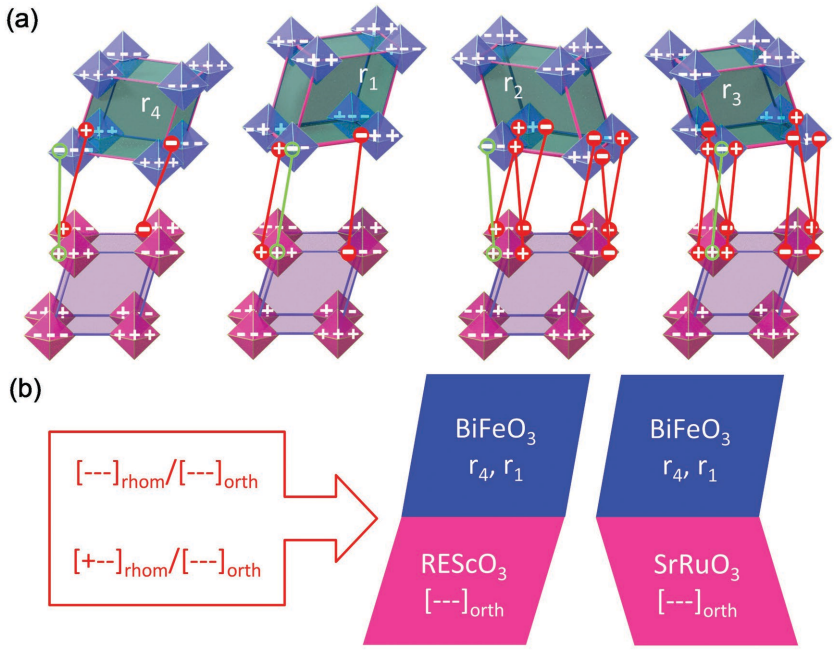


**Figure 3.** Interfacial-OOC-induced domain structure of rhombohedral ($a^-a^-a^-$) $BiFeO_3$ film on orthorhombic $(110)_{orth}$ substrate. a) Octahedral rotation signs network at the interface of $BiFeO_3$ and an orthorhombic $(110)_{orth}$ substrate. The $a^-a^-a^-$ Glazer tilt system has four different rotation networks $[---]_{rhom}$, $[+--]_{rhom}$, $[--+]_{rhom}$, and $[+-+]_{rhom}$. The green "⊸" highlight some of the matched tilt signs while all the unmatched tilt signs across interface are highlighted by red "⊸". b) Domain structures of $BiFeO_3$ films on orthorhombic $REScO_3$ and $SrRuO_3$ $(110)_{orth}$ substrates. Structures adapted from ref. [25–27].

If the OOC effect at a heterosymmetric interface is strong enough to induce a different OOR pattern in a film near the interface to match the substrate OOR, the initiated different symmetry can propagate away from the interface deeply into the full thickness of the films. An example is the structure of a LSMO film on an NGO $(110)_{orth}$ substrate. The bulk LSMO is rhombohedral ($a^-a^-a^-$), but the OOC effect at the LSMO/NGO interface is so strong that one out-of-phase rotation about the *a*-axis in LSMO near the interface (within ≈ 3 uc) is converted into in-phase ($a^-\rightarrow a^+$).[17] As a result, the near interface LSMO becomes orthorhombic. Although the effect of OOC on the magnitude of the octahedral tilt decays steeply within 4 uc,[17] the characteristic orthorhombic structure still survives over an extensive thickness range, resulting in an orthorhombic structure in thick LSMO films. The RSM of a 30 uc LSMO film shows that the LSMO film possesses an orthorhombic structure with $a^+b^-c^-$ Glazer notation ($P2_1/m$) (see **Figure 4**a).[15] The observed $\alpha_{LSMO} > 90°$ on $\alpha_{NGO} < 90°$ configuration indicates that the $[---]_{orth}$ network of LSMO corresponds to $\alpha > 90°$. The $\alpha_{LSMO} > 90°$ on $\alpha_{NGO} < 90°$ configuration growth is further microscopically revealed by the scanning transmission electron microscopy (STEM). STEM high angle annular dark field (HAADF) cross-section image shows that the unit cell of LSMO is relatively tilted with respect to the NGO unit cell (see Figure 4b). The relative tilt angle (defined by $\Delta\alpha$ as shown in the inset of Figure 4b) is estimated from the B-site positions which are determined using statistical parameter estimation theory (Figure S5, Supporting Information).[33] As shown in the plot of B site (X, Y) positions in Figure 4c, a sudden change of the slope occurs at the interface which cannot be due to image drift and is therefore ascribed to different monoclinic tilt angles in LSMO and NGO. A relative tilt of $\Delta\alpha = \tan^{-1}(k_{LSMO}) - \tan^{-1}(k_{NGO}) \approx 0.96 \pm 0.06°$ obtained from the STEM image, which agrees well the value of 1° extracted from RSM (See Figure 4a and Table S2, Supporting Information).

The strong impact of the OOC on the symmetry of perovskite heterostructures is further observed when engineering the symmetries through an additional buffer layer without varying the strain. By growing a fully strained $SrTiO_3$ (STO) film, which does not have tilt in its bulk form, on a NGO $(110)_{orth}$ substrate, one obtains a tetragonal STO buffer with $\alpha = \beta = \gamma = 90°$ (for details, see Figure S6, Supporting Information). Due to the compressive strain effect, the STO buffer layer exhibits $a^0a^0c^-$ structure according to X-ray diffraction measurements by He et al.[34] The LSMO film on this $a^0a^0c^-$ STO buffer layer exhibits a different symmetry from the LSMO directly on $c^+a^-a^-$ NGO substrate. The structure of the buffered LSMO is refined from RSM of the (024), (0–24), (204) and (–204) reflections (see Figure 4d), the $\alpha = \beta = \gamma = 90^0$ and $a < b < c$. Together with the fact that the tilt along the *a*-axis disappears in buffered LSMO,[17] only two Glazer tilt systems satisfy all these conditions: #15 $a^0b^+c^+$ and #19 $a^0b^+c^-$. Since the latter one $a^0b^+c^-$ doesn't change the out-of-phase rotation along c-axis moving from STO to LSMO and thus will be more favorable. We tentatively assign the $a^0b^+c^-$ to buffered LSMO.

The change of structure due to the STO buffer layer is also atomically visualized in STEM image shown in Figure 4e, where no relative unit cell tilt exists between LSMO and STO, although it is present at the STO/NGO interface. The relative tilt angle can be calculated using the B-site (X,Y) positions as shown in Figure 4f. A sudden change of the slope is observed when crossing the STO/NGO interface, due to the tetragonal structure of the STO on the orthorhombic NGO, but is absent at the LSMO/STO interface. The relative tilt angle $\Delta\alpha$ between LSMO/STO and NGO is about 0.76 ± 0.06°, in good agreement with the number obtained from RSM (see Table S2, Supporting Information). Thus, the mirror symmetry recovered in the STO layer is now transferred into the LSMO layer.

When only considering the strain effect, the LSMO can accommodate the in-plane strain induced by NGO via shaping its structure into either $a^0b^+c^-$ or $a^+b^-c^-$, which both can produce $a < b$ and $\gamma = 90°$ lattice parameters. Since the buffered and nonbuffered LSMO share the same strain (see Figure 4a,d), the observed different symmetries of buffered and nonbuffered LSMO films on NGO further supports the central role of the OOC mediated symmetry propagation effect in determining the structure of perovskite heterostructures. A similar effect is observed in $NdNiO_3$ (NNO)/STO/NGO $(110)_{orth}$ (see **Figure 5**a) and SRO/STO/DSO $(110)_{orth}$ (see Figure S6,



*Adv. Funct. Mater.* **2016**,
DOI: 10.1002/adfm.201602155

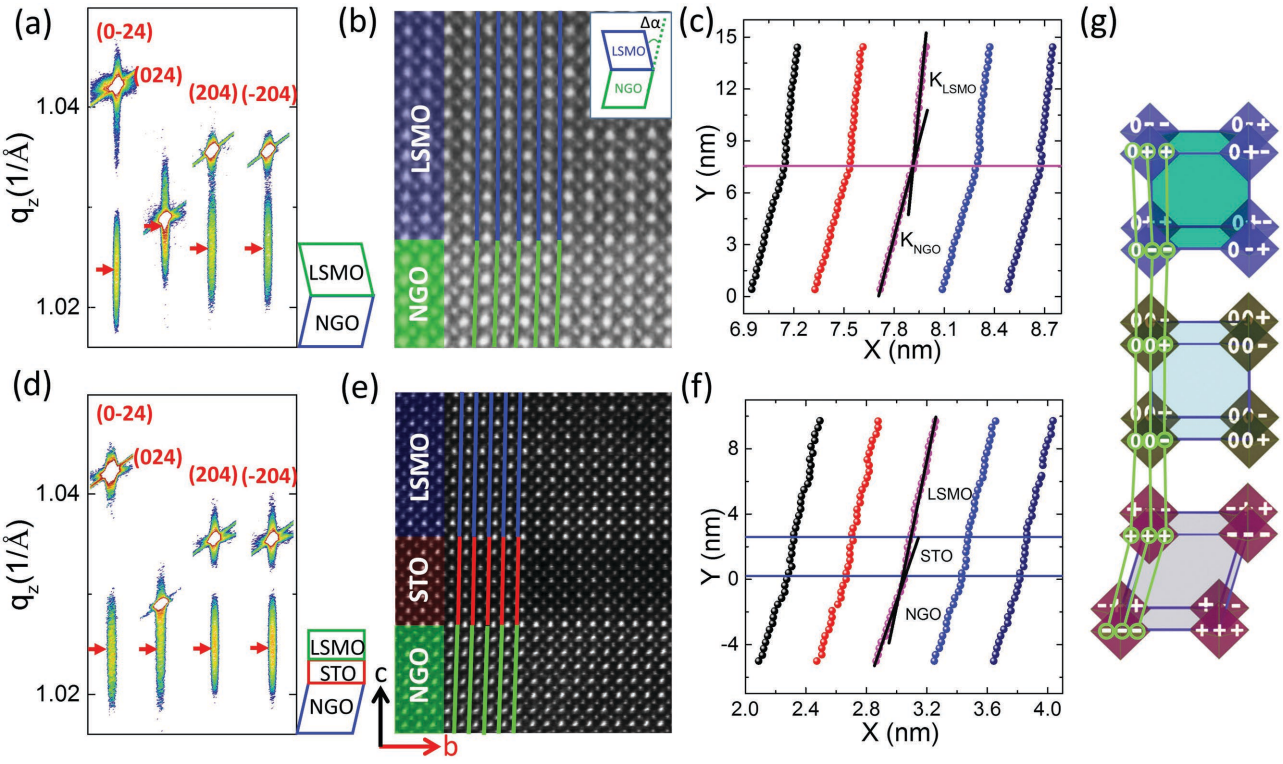


**Figure 4.** Tailoring structure by interface symmetry engineering. RSM of LSMO films a) with and d) without 6 uc STO buffer layers. HAADF cross-section image of 30 uc LSMO films b) with and e) without 6 uc STO buffer layers. Inset image at top-right corner of (b) indicates the definition of relative unit cell tilt angle $\Delta\alpha$. c) The positions (X, Y) of B site atoms from five columns marked by lines in panel (b). K represents the slope of the curve. f) The positions (X, Y) of B site atoms from five columns marked by lines in panel (e). g) Octahedral rotation signs network in LSMO/STO/NGO heterostructure.

Supporting Information). With an additional STO buffer layer, the orthorhombic NNO and SRO are switched to tetragonal structures. (see Table S2, Supporting Information). Taking nontilt ($a^0$) as in-phase or out-of-phase but with zero tilt angle ($0^+$ or $0^-$), then the nontilt behavior can match both the in-phase and out-of-phase in aspect of symmetry. A decay of the tilt angle from finite value to zero naturally maintains the connectivity of the octahedra.[17] Based on this, a continuous connection of octahedra across LSMO/STO/NGO heterostructure can be drawn as shown in Figure 4g.

It is noteworthy that the intrinsic chemical pressure from A and B site atoms, quantified by the tolerance factor $t = (r_A+r_O)/\sqrt{2}(r_B+r_O)$[35] and the strain would also strongly affect the rotation pattern[15] and thus interfere with the interfacial OOC effect. Which effect is energetically dominant strongly depends on the structure, chemical bonding nature of the films and substrates. For example, the BFO films prefer bulk rhombohedral structure[25–27] while the LSMO film will be easily changed from bulk rhombohedral to orthorhombic or tetragonal structure depending on the substrate strain and symmetry. How the OOC competes with other effects would require further theoretical investigation. According to our results, even when the intrinsic chemical pressure dominates over epitaxial growth in determining their crystal symmetry, the interfacial OOC effect can still affect the domain structures, e.g., BFO/RSO as discussed above, CTO/NGO and CTO/STO/NGO [see Figure S6, Supporting Information]. If the OOC is strong enough to induce a new symmetry, then this new symmetry can be propagated much deeper into the film than the OOC induced tilt angle.

The OOC is usually considered as an effect to modify the octahedral tilt angle over a very short range length scale of 4–8 uc, however, its long range impact on domain structure and symmetry has a much more profound

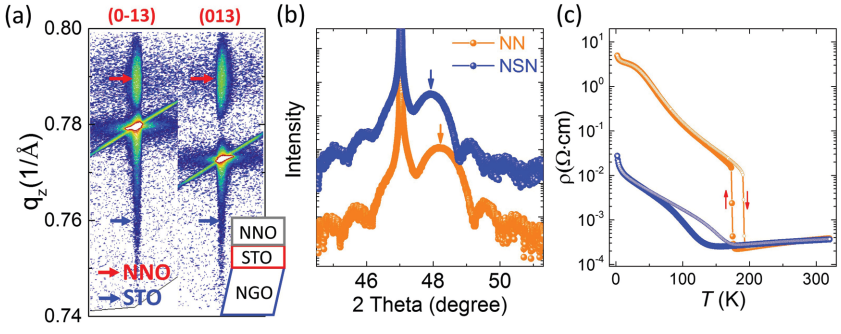


**Figure 5.** Manipulating the metal-to-insulator transition in $NdNiO_3$ film. a) RSM of 6 uc STO buffered 30 uc NNO film on NGO substrate. b) Theta-2 Theta scan of a 30 uc NNO film on NGO without (NN) and with (NSN) a 6 uc STO buffer layer. The arrows indicate the peak position of NNO $(002)_{pc}$. c) Temperature dependent resistivity of NNO films with and without STO buffer layer. The cooling and warming data are shown by big solid spheres (darker color) and smaller open circles (lighter), respectively.

impact on the properties of a film. Figure 5b shows the XRD results of 30 uc NNO films on NGO $(110)_{orth}$ substrates without (labeled NN) and with (labeled NSN) a 6 uc STO buffer layer. The shift in the NNO (002) peak position for NSN as compared to that for NN indicates a larger out-of-plane lattice constant. Since the OOC induced the change of tilt angle is quite limited to only the interfacial region, the change of the lattice constant in a 30 uc NNO films is attributed to a change in symmetry. The orthorhombic NNO films on NGO possesses triple tilts ($b^+c^-a^-$) while the tensile strained and tetragonal NNO on $a^0a^0c^-$ STO buffer layer is a dual-tilts system ($a^+b^+a^0$).[36] We use $b^+c^-a^-$ for orthorhombic NNO and $a^+b^+a°$ for tetragonal NNO instead of ($a^+b^-b^-$) and $b^+b^+a°$,[36] respectively, by considering the fact of unequal three lattice parameters $c < a < b$. Concomitant to change of structure, the metal to insulator transition (MIT) and conductivity of the films are quite different as can be seen in Figure 5c. The MIT temperature ($T_{MIT}$) in nonbuffered NNO is ≈182 K, similar to previously reported values in bulk and films,[37–39] but with a STO buffer layer, the $T_{MIT}$ is significantly lowered down to ≈149 K. At low temperatures ($T$ < 150 K), the resistivity of the buffered NNO is almost two orders of magnitude less that of nonbuffered NNO (see Figure 5c).

To further investigate the impact of this change of symmetry on the electronic and magnetic structure of the NNO films, we performed X-ray absorption spectroscopy (XAS) and resonant magnetic diffraction (RMD) measurements.[40] **Figure 6**a shows the temperature-dependent Ni $L_3$-edge XAS of the NSN and NN samples. The main features of the XAS—two primary peaks at low temperatures in the insulating regime, which merge together at higher temperatures in the metallic regime—are consistent with previous reports on bulk nickelates.[41] However, the fine details of the two samples are distinctly different. For the STO-buffered film, the two primary peaks are closer together, which is comparatively similar to $PrNiO_3$ (PNO) in the bulk phase diagram.[41] This is consistent with the reduced OOR due to the symmetry imposed by the STO layer. By going from bulk NNO to PNO in the nickelate phase diagram, octahedral rotations are also reduced and the $T_{MIT}$ shifts to lower temperatures,[41] as observed in our symmetry-engineered films.

Figure 6a also shows the energy dependence of the RMD signal at the Ni $L_3$ resonance. The signal arises from the (1/4,1/4,1/4) magnetic Bragg reflection, indicative of the E'-type antiferromagnetic ordering of the nickelates. For both films, we find a robust diffraction signal at 22 K, with an energy dependence similar to what has been measured for other nickelates.[42,43] In Figure 6b, we show the temperature dependence of the RMD signal, with the X-ray energy tuned to that of the $L_3$ resonance maximum. Similar to what was observed for the MIT, we find that the symmetry change imposed by the STO buffer layer reduces the Néel temperature ($T_N$) of the NNO film from 180 K down to ≈150 K.

Oxygen K-edge XAS, shown in Figure 6c, provides a measurement of the Ni–O covalency in the films. The strong prepeak near 528.5 eV originates from excitations into strongly hybridized Ni 3d – O 2p unoccupied states just above the Fermi level. For the buffered NNO, the prepeak is wider (full width at half maximum (FWHM) of 1.2 eV versus 1.1 eV as indicated by the arrows for each case) and is pushed to a slightly higher energy, both consistent with a wider bandwidth due to the reduction in OOR for the buffered film. A spectrum from a pure $SrTiO_3$ crystal is shown as well, verifying that a signal from the STO buffer layer does not contribute to the prepeak region and only adds a small bump at higher energies. The observed increase of the bandwidth due to the STO buffer layer is possibly the driving force[37,41,44] for enhanced conductivity and reduced Néel temperature in the buffered NNO film. Although the exact mechanism for the MIT in NNO films is complex and still a matter of debate,[37–45] our finding of the impact of structure on $T_{MIT}$ and $T_N$ suggests that the OOR which controls the electron bandwidth could play a vital role.[37] Therefore, the symmetry change imposed by the $SrTiO_3$ buffer layer moves the NNO film significantly across the nickelate phase diagram—as evidenced by the resistivity, magnetism, and general electronic structure—providing a unique and new way of tuning the macroscopic properties.

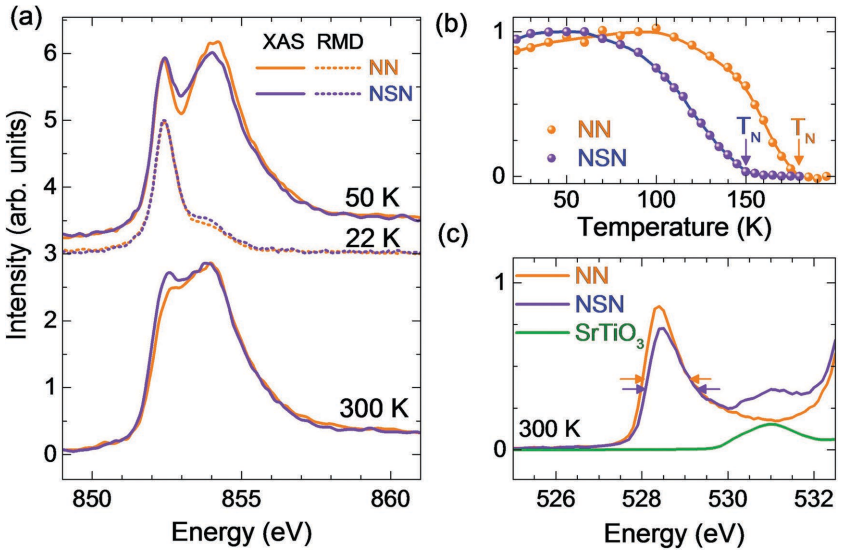


**Figure 6.** Electronic structure and antiferromagnetic ordering in $NdNiO_3$ films. a) Ni $L_3$-edge X-ray absorption (XAS) and resonant magnetic diffraction (RMD) for unbuffered (labeled NN) and STO buffered (labeled NSN) 30 uc NNO on NGO. b) Temperature dependence of the magnetic diffraction intensity. The arrows indicate the Néel temperature, showing a decrease in the Néel temperature for the buffered film. c) Oxygen K-edge spectra of the same samples at 300 K, showing an increased bandwidth for the buffered sample.

The control of properties by the engineering of symmetry propagation is found also in LSMO films (for details, see Figure S7, Supporting Information). A 6 uc STO buffered 30 uc LSMO film is much more conductive and has higher Curie temperature than a nonbuffered LSMO film. Previously reported substrate symmetry effects involving materials such as LSMO[20] or NNO[39] were achieved by using different substrates of NGO $(001)_{orth}$, NGO $(110)_{orth}$, or $(LaAlO_3)_{0.3}(Sr_2TaAlO_6)_{0.7}$ (LSAT) (001), where a small difference in lattice mismatch always exists, hence the effect of strain cannot be



Adv. Funct. Mater. 2016,
DOI: 10.1002/adfm.201602155

fully ruled out. As there is no modification of the strain but solely an engineering of the symmetry of the film, our results unambiguously reveal the strong impact of long range symmetry propagation on properties and functionalities. This long range variation of symmetry enforced by an ultrathin buffer layer also indicates the capability to tailor structure and their properties at unit cell thickness level. Since the octahedral rotation can also cause an octahedral distortion,[14] in addition to a change of the octahedral tilt, such control of the symmetry can be used for engineering of magnetic anisotropy,[46] orbital ordering,[47] ferroelectricity,[48] and magnetism.[49]

## 3. Conclusion

In conclusion, we have illustrated a strong role of interfacial OOC in affecting the domain structure or crystalline symmetry of epitaxial films. The long range effect of local OOC on structures enables us to engineer the domain structure or symmetry of oxide heterostructures in a flexible way by using either homosymmetric or heterosymmetric interfaces. The interfacial OOC initiates structure propagating over extensive distances and subsequently allows us to tune the structure of epitaxial films by locally varying the substrate symmetry via the insertion of an ultrathin buffer layer. The octahedral network is common in all perovskite heterostructures, hence our findings provide a deep insight into understanding structure-properties relation in perovskite heterostructures and superlattices. The OOC mediated long-range structure propagation also provides us with a new strategy to engineer structure and functionalities in oxide heterostructure over distances comparable of that of the strain. The visualized connectivity of the rotation pattern across interface as we have developed also provides us a convenient method to analyze the symmetry mismatch and anticipate the resultant film structure

## 4. Experimental Section

The perovskite oxide films were grown by pulsed layer deposition on single terminated NGO and DSO substrates. The single terminated NGO and DSO surfaces were obtained by a combined chemical etching and subsequent high temperature annealing (more details can be found in the Supporting Information). Reflection high energy electron diffraction was used to accurately control the individual layer thicknesses. Transport properties were characterized by quantum design physics property measurement system. The lattice structures of the thin films were determined by PANalytical-X'Pert materials research diffractometer at high resolution mode. Atomic scale characterization of the lattice structure was performed by Cs-corrected STEM on the X-Ant-Em instrument at the University of Antwerp. Cross-sectional cuts of the samples along the NGO $[1\text{-}10]_{orth}$ direction were prepared using a FEI Helios 650 dual-beam Focused Ion Beam device.

The XAS and RMD were performed using an in-vacuum 4-circle diffractometer at the resonant elastic and inelastic X-ray scattering beamline at Canadian light source in Saskatoon, Canada. The beamline has a flux of $5 \times 10^{12}$ photon $s^{-1}$ and photon energy resolution of $10^{-4}$ eV. The base pressure of the diffractometer chamber was kept lower than $10^{-9}$ Torr. The XAS spectra were measured using the total fluorescence yield method, with the incident photons at an angle of 30° from the surface. At the Ni $L_3$ edge, $\pi$-polarized photons were used (polarization vector within the sample $a$–$c$ pseudocubic plane), while at the oxygen K edge, measurements with $\pi$ and $\sigma$ polarizations were averaged.

## Supporting Information

Supporting Information is available from the Wiley Online Library or from the author.

## Acknowledgements

The authors thank B. Keimer for valuable discussions. M.H., G.K., and G.R. acknowledge funding from DESCO program of the Dutch Foundation for Fundamental Research on Matter (FOM) with financial support from the Netherlands Organization for Scientific Research (NWO). This work was funded by the European Union Council under the 7th Framework Program (FP7) Grant No. NMP3-LA-2010-246102 IFOX. J.V. and S.V.A. acknowledge financial support from the Research Foundation Flanders (FWO, Belgium) through project fundings (G.0044.13N, G.0374.13N, G.0368.15N, G.0369.15N). The Qu-Ant-EM microscope was partly funded by the Hercules fund from the Flemish Government. N.G. acknowledges funding from the European Research Council under the 7th Framework Program (FP7), ERC Starting Grant 278510 VORTEX. N.G., J.G., S.V.A., J.V. acknowledge financial support from the European Union under the Seventh Framework Program under a contract for an Integrated Infrastructure Initiative (Reference No. 312483-ESTEEM2). The Canadian work was supported by the NSERC and the Max Planck-UBC Centre for Quantum Materials. Some experiments for this work were performed at the Canadian Light Source, which was funded by the Canada Foundation for Innovation, NSERC, the National Research Council of Canada, the Canadian Institutes of Health Research, the Government of Saskatchewan, Western Economic Diversification Canada, and the University of Saskatchewan.

Received: April 29, 2016
Revised: May 24, 2016
Published online:

[1] P. W. Anderson, *Basic Notions of Condensed Matter Physics*, Westview Press, Boulder, CO, USA **1997**.
[2] V. Gopalan, D. B Litvin, *Nat. Mater.* **2011**, *10*, 376.
[3] C. C. Tsuei, J. R. Kirtley, *Rev. Mod. Phys.* **2000**, *72*, 969.
[4] X. L. Qi, S. C. Zhang, *Rev. Mod. Phys.* **2011**, *83*, 1057.
[5] R. Schelkens, *Phys. Status Solidi B* **1970**, *37*, 739.
[6] A. S. Disa, D. P. Kumah, A. Malashevich, H. H. Chen, D. A. Arena, E. D. Specht, S. Ismail-Beigi, F. J. Walker, C. H. Ahn, *Phys. Rev. Lett.* **2015**, *114*, 026801.
[7] M. P. Warusawithana, E. V. Colla, J. N. Eckstein, M. B. Weissman, *Phys. Rev. Lett.* **2003**, *90*, 036802.
[8] H. N. Lee, H. M. Christen, M. F. Chisholm, C. M. Rouleau, D. H. Lowndes, *Nature* **2005**, *433*, 395.
[9] J. Wang, J. B. Neaton, H. Zheng, V. Nagarajan, S. B. Ogale, B. Liu, D. Viehland, V. Vaithyanathan, D. G. Schlom, U. V. Waghmare, N. A. Spaldin, K. M. Rabe, M. Wuttig, R. Ramesh, *Science* **2003**, *299*, 1719.
[10] H. Boschker, J. Kautz, E. P. Houwman, W. Siemons, D. H. A. Blank, M. Huijben, G. Koster, A. Vailionis, G. Rijnders, *Phys. Rev. Lett.* **2012**, *109*, 157207.
[11] T. Z. Ward, J. D. Budai, Z. Gai, J. Z. Tischler, L. Yin, J. Shen, *Nat. Phys.* **2009**, *5*, 885.
[12] A. M. Glazer, *Acta Crystallogr.* **1972**, *B28*, 3384.
[13] C. J. Howard, H. T. Stokes, *Acta Crystallogr.* **1998**, *B54*, 782.

[14] P. M. Woodward, *Acta Crystallogr.* **1997**, *B53*, 32.
[15] A. Vailionis, H. Boschker, W. Siemons, E. P. Houwman, D. H. A. Blank, G. Rijnders, G. Koster, *Phys. Rev. B* **2011**, *83*, 064101.
[16] J. M. Rondinelli, S. J. May, J. W. Freeland, *MRS Bull.* **2012**, *37*, 261.
[17] Z. Liao, M. Huijben, Z. Zhong, N. Gauquelin, S. Macke, R. J. Green, S. V. Aert, J. Verbeeck, G. V. Tendeloo, K. Held, G. A. Sawatzky, G. Koster, G. Rijnders, *Nat. Mater.* **2016**, *15*, 425.
[18] D. Kan, R. Aso, R. Sato, M. M. Haruta, H. Kurata, Y. Shimakawa, *Nat. Mater.* **2016**, *15*, 432
[19] J. He, A. Y. Borisevich, S. V. Kalinin, S. J. Pennycook, S. T. Pantelides, *Phys. Rev. Lett.* **2010**, *105*, 227203.
[20] E. J. Moon, P. V. Balachandran, B. J. Kirby, D. J. Keavney, R. J. Sichel-Tissot, C. M. Schlepütz, E. Karapetrova, X. M. Cheng, J. M. Rondinelli, S. J. May, *Nano Lett.* **2014**, *14*, 2509.
[21] E. J. Moon, R. Colby, Q. Wang, E. Karapetrova, C. M. Schlepütz, M. R. Fitzsimmons, S. J. May, *Nat. Commun.* **2014**, *5*, 5710.
[22] D. G. Schlom, L.-Q. Chen, C.-B. Eom, K. M. Rabe, S. K. Streiffer, J.-M. Triscone, *Ann. Rev. Mater. Res.* **2007**, *37*, 589.
[23] D. L. Proffit, H. W. Jang, S. Lee, C. T. Nelson, X. Q. Pan, M. S. Rzchowski, C. B. Eom, *Appl. Phys. Lett.* **2008**, *93*, 111912.
[24] P. F. Chen, B. B. Chen, X. L. Pan, H. R. Xu, X. F. Xuan, Z. Guo, F. Jin, W. B. Wu, *Appl. Phys. Lett.* **2013**, *103*, 262402.
[25] F. Johann, A. Morelli, D. Biggemann, M. Arredondo, I. Vrejoiu, *Phys. Rev. B* **2011**, *84*, 094105.
[26] C. M. Folkman, S. H. Baek, H. W. Jang, C. B. Eom, C. T. Nelson, X. Q. Pan, Y. L. Li, L. Q. Chen, A. Kumar, V. Gopalan, S. K. Streiffer, *Appl. Phys. Lett.* **2009**, *94*, 251911.
[27] Z. H. Chen, A. R. Damodaran, R. Xu, S. Lee, L. W. Martin, *Appl. Phys. Lett.* **2014**, *104*, 182908.
[28] A. Beran, E. Libowitzky, T. Armbruster, *Can. Mineral.* **1996**, *34*, 803.
[29] L. Vasylechko, L. Akselrud, W. Morgenroth, U. Bismayer, A. Matkovskii, D. Savytskii, *J. Alloys Compd.* **2000**, *297*, 46.
[30] B. Velickov, V. Kahlenberg, R. Bertram, M. Bernhagen, *Z. Kristallogr.* **2007**, *222*, 466.
[31] J. S. Gardner, G. Balakrishnan, D. McK. Paul, *Phys. C* **1995**, *252*, 303.
[32] T. Ito, T. Ushiyama, Y. Yanagisawa, R. Kumai, Y. Tomioka, *Cryst. Growth Des.* **2011**, *11*, 5139.
[33] A. J. den Dekker, J. Gonnissen, A. De Backer, J. Sijbers, S. Van Aert, *Ultramicroscopy* **2013**, *134*, 34.
[34] F. Z. He, B. O. Wells, S. M. Shapiro, *Phys. Rev. Lett.* **2005**, *94*, 176101.
[35] R. S. Roth, *J. Res. Natl. Bur. Stand. (U.S.)* **1957**, *58*, 75.
[36] J. Y. Zhang, H. Y. Kim, E. Mikheev, A. J. Hauser, S. Stemmerm, *Sci. Rep.* **2015**, *6*, 23652.
[37] J.-S. Zhou, J. B. Goodenough, B. Dabrowski, *Phys. Rev. Lett.* **2005**, *95*, 127204.
[38] R. Scherwitzl, P. Zubko, I. G. Lezama, S. Ono, A. F. Morpurgo, G. Catalan, *Adv. Mater.* **2010**, *22*, 5517.
[39] X. K. Lian, F. Chen, X. Tan, P. Chen, L. Wang, G. Y. Gao, S. W. Jin, W. B. Wu, *Appl. Phys. Lett.* **2013**, *103*, 172110.
[40] D. G. Hawthorn, F. He, L. Venema, H. Davis, A. J. Achkar, J. Zhang, R. Sutarto, H. Wadati, A. Radi, T. Wilson, G. Wright, K. M. Shen, J. Geck, H. Zhang, V. Novák, G. A. Sawatzky, *Rev. Sci. Instrum.* **2011**, *82*, 073104.
[41] J. W. Freeland, M. V. Veenendaal, J. Chakhalian, Evolution of Electronic Structure Across the Rare-Earth RNiO3 Series, arXiv: 1504.02802.
[42] A. Frano, E. Schierle, M. W. Haverkort, Y. Lu, M. Wu, S. Blanco-Canosa, U. Nwankwo, A. V. Boris, P. Wochner, G. Cristiani, H. U. Habermeier, G. Logvenov, V. Hinkov, E. Benckiser, E. Weschke, B. Keimer, *Phys. Rev. Lett.* **2013**, *111*, 106804.
[43] V. Scagnoli, U. Staub, A. M. Mulders, M. Janousch, G. I. Meijer, G. Hammerl, J. M. Tonnerre, N. Stojic, *Phys. Rev. B* **2006**, *73*, 100409(R).
[44] J. Liu, M. Kargarian, M. Kareev, B. Gray, P. J. Ryan, A. Cruz, N. Tahir, Y. D. Chuang, J. H. Guo, J. M. Rondinelli, J. W. Freeland, G. A. Fiete, J. Chakhalian, *Nat. Commun.* **2013**, *4*, 2714.
[45] J. Liu, M. Kareev, D. Meyers, B. Gray, P. Ryan, J. W. Freeland, J. Chakhalian, *Phys. Rev. Lett.* **2012**, *109*, 107402.
[46] H. Boschker, M. Mathews, E. P. Houwman, H. Nishikawa, A. Vailionis, G. Koster, G. Rijnders, D. H. A. Blank, *Phys. Rev. B* **2009**, *79*, 214425.
[47] T. Mizokawa, D. I. Khomskii, G. A. Sawatzky, *Phys. Rev. B* **1999**, *60*, 7309.
[48] N. A. Benedek, C. J. Fennie, *Phys. Rev. Lett.* **2011**, *106*, 107204.
[49] N. Ganguli, P. J. Kelly, *Phys. Rev. Lett.* **2014**, *113*, 127201.



*Adv. Funct. Mater.* **2016**,
DOI: 10.1002/adfm.201602155